# Multi-direction bending sensing based on spot pattern demodulation of dual-hole fiber

Boyao Li (李波瑶)[1]*, Yaoyao Liang (梁瑶瑶)[2], Zhongye Xie (谢仲业)[1], Xiaojie Zuo (左小杰)[1], and Jinghua Sun (孙敬华)[1]

[1] School of Electronic Engineering and Intelligentization, Dongguan University of Technology, Dongguan 523808, China
[2] Centre de Nanosciences et de Nanotechnologies, CNRS, Université Paris-Saclay, C2N, 91120 Palaiseau, France

A multi-direction bending sensor based on spot pattern demodulation of a dual-hole fiber (DHF) is proposed. By using the interference and scattering in a DHF, the related multidirectional variations can be captured by the optical field. Furthermore, the multi-directional bending characteristics of the fiber are quantitatively described by the pattern of the output light spot, achieving multidirectional bending sensing. In addition, considering the subtle changes in the deformation patterns over time, a convolutional neural network (CNN) model based on deep learning is introduced for accurate recognition and prediction of the bending angle. The experimental results show that the sensor can perceive different bending angles in four directions. These outstanding results indicate that the multi-directional bending sensor based on dual-hole interference pattern decoding has potential applications in multi-directional quantitative sensing and artificial intelligence perception.

## 1. Introduction

Bending sensors have been used in many fields, such as mechanical engineering, structural monitoring, and astronautics[1–3]. Meanwhile, optical fiber has become a natural carrier for sensors due to its advantages of flexible transmission, integration, and resistance to electromagnetic interference[4,5]. Therefore, in the past few years, many types of fiber bending sensors have been reported based on fiber gratings[6,7], photonic crystal fibers (PCFs)[8,9], Mach–Zehnder interferometers[10,11], multi-core fiber sensors[12,13], S-shaped bending fiber sensors[14], and others. The main principle of these works is to use information such as the position changes of the characteristic peaks in the transmission spectrum after pattern interference to ultimately obtain the corresponding bending information. In order to improve sensing performance, in 2019, Zheng et al. achieved better bending detection results by using the large-mode-field area of the hollow core fiber and fusing it with a single-mode fiber, both theoretically and experimentally[15].

However, in the actual monitoring of the bending, one or two simple bending directions cannot fully reflect the actual situation, so it is necessary to monitor bending in multiple directions. For realizing the multi-direction bending detection, two or more bending sensors are usually used with complex fabrications. In practical applications, it is favorable to reduce the number of sensors when measuring the bending radius or other parameters.

Thus, Guan et al. improved the fiber structure to reflect the bending in both directions from the spectrum[16]. Furthermore, a number of one-dimensional bending direction sensing units can be compactly integrated into a multicore fiber (MCF) to realize two-dimensional bending sensing[17,18]. Nevertheless, spectral information can only describe the wavelength of light, and it is easy to generate spectral overlap corresponding to multiple spatial vector directions, which is difficult to demodulate. In addition, compared to spectrum information, the light spot itself carries more information and is easier to obtain[19].

Therefore, we report a method based on spot pattern demodulation in a dual-hole fiber (DHF) to realize multi-direction bending sensing. Due to defects in the fiber structure, the scattered light field transmitted internally emits a highly sensitive spatial interference pattern. Compared to speckle patterns in Ref. [19], interference fringes are more regular and precise. Moreover, due to the asymmetry of the structure, the spatial distribution of the light spot pattern is also directional, which is very conducive to multi-directional fiber bending judgment. Through the analysis of a convolutional neural network for combining classification and regression, more than 98% accuracy can be achieved in determining the bending direction and angle simultaneously among 128 group test spot patterns. It provides potential application value for subsequent multi-dimensional bending detection, beam light modulation, etc.

## 2. Experiments

Figure 1(a) shows the sensor's 3D view schematic diagram. Light passing through the sensor can form a spot pattern in the space of the rear end face of the double-hole fiber (DHF). By collecting the spot pattern, the bending situation can be further determined. The principal diagram of the sensing device and relative sensing mechanism is shown in Fig. 1(b). When light is transmitted into a single-mode fiber, it undergoes scattering due to structural changes after passing through a DHF (in S1 region). Then, the light propagates along the high-refractive-index cladding (in S2 region). Finally, the scattered light from the cladding forms an interference speckle pattern in space (in S3 region). During the fiber bending process (in S2 region), different bending radii affect the refractive index of the fiber as follows:

$$n'(x, y) = (1 + x/R_{eff})n(x, y). \qquad (1)$$

In Eq. (1), the $x$- and $y$-axes are in the local transverse fiber plane. $R_{eff}$ is the equivalent bending radius, and $n(x, y)$ is the refractive index of the straight fiber cross section[20,21]. When two beams of light ($I_1$, $I_2$) transmitted in the DHF interfere, they experience different optical paths $d(x, y) = L \times n'(x, y)$, and the final intensity ($I_t$) of the interference is

$$I_t = I_1 + I_2 + 2 \times \sqrt{I_1 I_2} \cos\left(\frac{\delta d(x,y)}{\lambda} 2\pi\right). \qquad (2)$$

where $\lambda$ and $L$ are the wavelength of the incident light and the geometric length of the part of the light passing through the bent fiber, respectively. Moreover, $\delta d(x, y)$ is the optical path difference between different paths. Figure 1(c) is the cross section of the DHF. The diameters of the DHF and the hole are 218 µm and 20 µm, respectively. The double hole spacing of the DHF
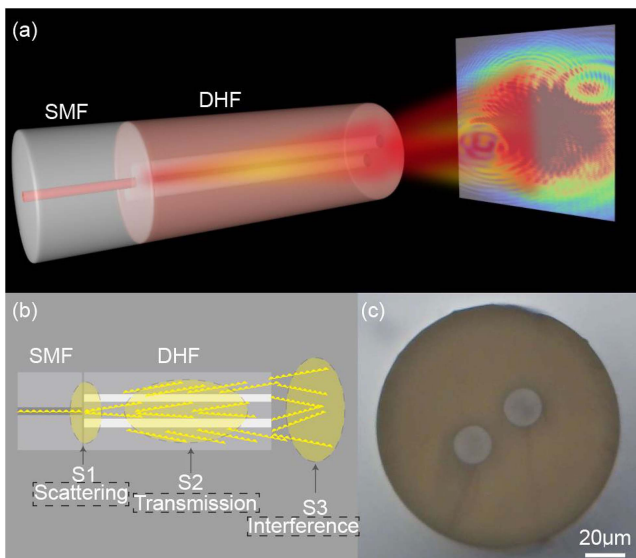


**Fig. 1.** Schematic diagram of the design and principle of the DHF sensor. (a) The 3D schematic diagram of the proposed sensor. (b) The schematic illustration of the sensing principle. (c) Cross section of the fabricated DHF.

is 38 µm. The sizes and spacing of the two holes are not too large, which is conducive to the concentrated distribution of interference light and facilitates signal collection.

## 3. Results and Discussion

### 3.1. DHF light field simulation and bending experimental results of the spot pattern

For accurately describing the spot distribution performance of DHF, the finite element simulation method (FEM) was used to calculate the transmission characteristics of the sensor. The relative analysis is based on the beam envelope module in the general numerical analysis tool. The geometry of model is the $x$–$z$ cross section of structure in Fig. 1(a). The related results in Fig. 2(a) show the scattering of light in the DHF and interference in space. We selected two different positions p1 and p2 to analyze their spot distribution. Clearly, as shown in Fig. 2(b), the spatial interference distribution after the end face of the DHF is related to the distance from the end face of the DHF. This also means that the effect of bending is different when observing the light spot of the DHF at different positions after the end face of the fiber, and appropriate choices need to be made in terms of light spot intensity and corresponding stripe resolution. In addition, the lateral profile of the light spot at a given position was analyzed, as shown in Fig. 2(c). Due to the asymmetry of the DHF structure, the corresponding light spot is severely modulated by the double holes where the fiber core is located, breaking the original circular symmetry. In addition, due to the influence of the interference, the distribution of the fringes is also observed, which has excellent characteristics for subsequent resolution of fiber structure bending.

In addition, the influence of DHF on temperature during the bending process also needs to be considered. The dual-hole optical fiber used in the manuscript is made of a silicon dioxide material. The thermal optical coefficient of the silicon dioxide is in the order of $10^{-5}$ at a temperature of around 30°C. So theoretically, when fiber length is around tens of centimeters and the temperature change is within the range of 10°C, the temperature has little effect on the refractive index of the transmission mode of the DHF. Figure 3 is a comparison graph of DHF at different temperatures. By subtracting the collected graphs, the similarities and differences between the two graphs are compared. Figure 3 shows that there is no significant change in the image from the room temperature (27°C) to 35°C (corresponding to the pixel subtraction of 0 pixels and black pixels). This indicates that the DHF has good stability within a certain temperature range. The experimental results in this work were also tested at room temperature, and the temperature change throughout the process did not exceed 2°C. So the influence of the temperature on the optical fiber spot can be ignored at room temperature or with small temperature fluctuations.

Based on above characteristics of the sensor, the spatial distribution patterns with different bending angles and directions were sampled and analyzed. The principle of the bending device
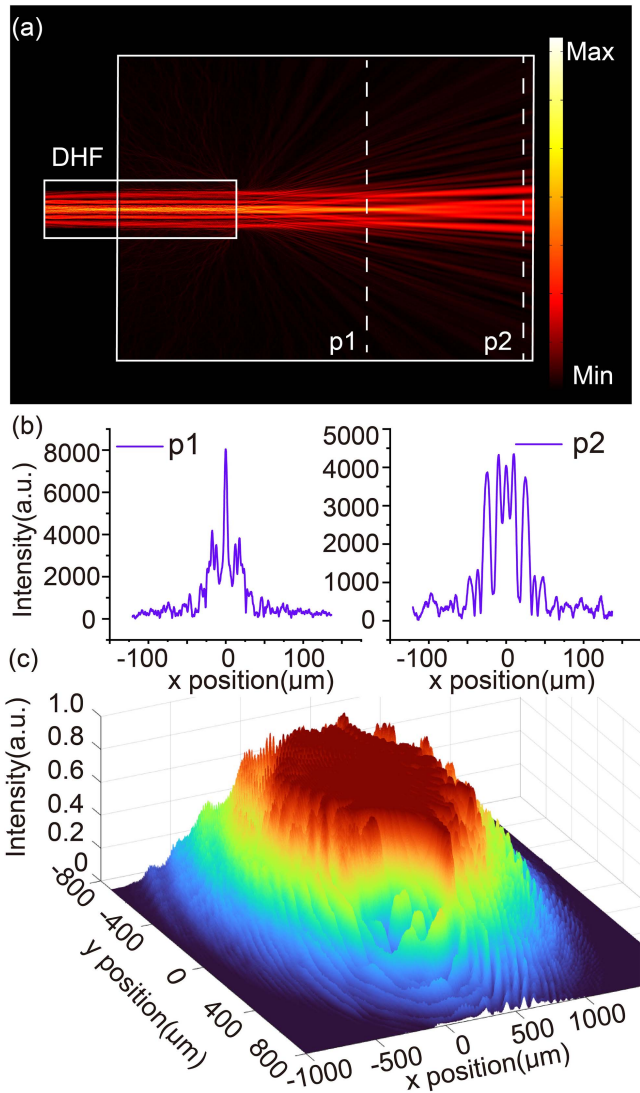
**Fig. 2.** Numerical and experimental results of the sensor. (a) The side beam propagation diagram of the numerical simulation of the device. (b) The light intensity distribution at different spaces between DHF and CCD. (c) The experimental transmission results when the distance between the end of the DHF and the receiving CCD is 3 cm.
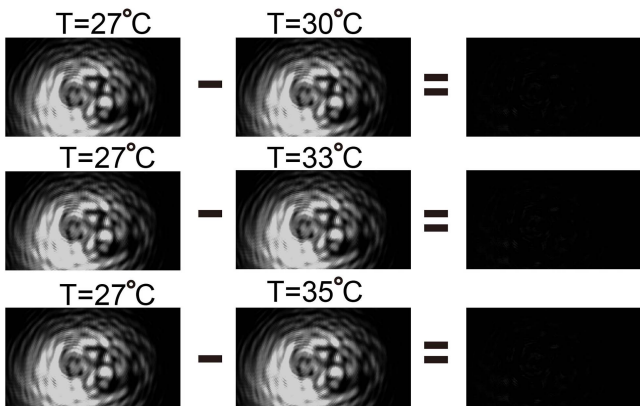


**Fig. 3.** The influence of temperature changes on the light spots.

is as shown in Fig. 4(a). We fixed the ruler on the end of the holder, and on another end of the ruler, we fixed a three-dimensional adjusting setup. The DHF is attached to the surface of the ruler. Then, the bending radius of the DHF can be controlled by the distance between both ends of the ruler and can be calculated as

$$\frac{S}{2R} = \arcsin\left(\frac{S - \mathrm{d}s - \mathrm{d}p}{2R}\right), \tag{3}$$

where $S$ represents the length of ruler, and $\mathrm{d}s$ and $R$ are the displacement and bending radius, respectively. Moreover, $\mathrm{d}p$ is the pre-moved position of the ruler. In this Letter, $S$ is 30 cm. In order to ensure the stability of the bending structure, the device first moves 2 cm and then moves from 0.01 mm to 0.09 mm to change the bending radius (i.e., $\mathrm{d}p$ is 2 cm and $\mathrm{d}s$ is selected from 0.01 mm to 0.09 mm). So the bending radius has been reduced from 333.55 mm to 326.38 mm. The settings for the different bending directions are shown in the illustration on the right side of Fig. 4(a). First, confirm the position of the DHF double holes under the microscope. Then, stick adhesive tape on the side of the fiber parallel to the double holes so that the position of the double holes can be identified from the offset direction of the tape. We define the directions parallel to the double hole connection as "up" and "down," and the vertical directions as "left" and "right." Ultimately, by rotating the DHF, the specific bending direction can be determined. It should be noted that due to the simultaneous operation of the straightedge bending device and the device for rotating the fiber bending direction, we only
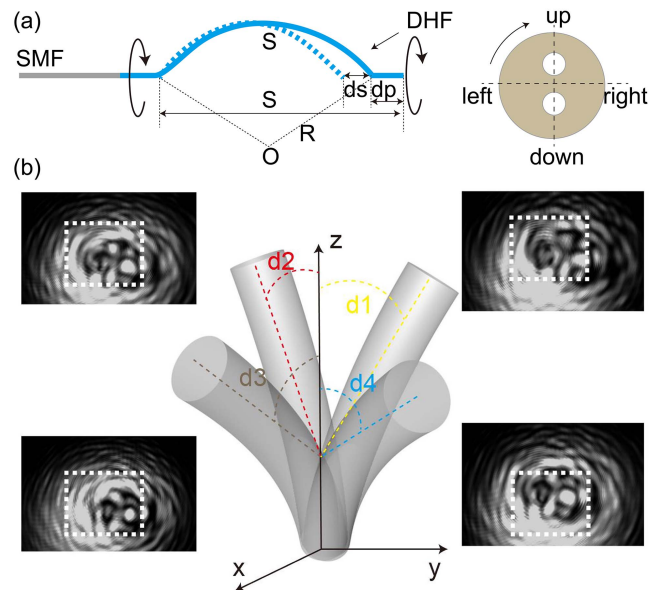


**Fig. 4.** Bending experimental principle and results. (a) The light of the customized laser (980 nm) goes through the SMF to the DHF, and the final signal was recorded by the CCD (Ncam). The bending radius can be controlled by regulating the distance of $\mathrm{d}s$. As for the different bending directions, it can be achieved by rotating the DHF. (b) The light spot patterns corresponding to bending at different directions with the same radius. $d_1$, $d_2$, $d_3$, and $d_4$ represent the four directions of "up," "left," "down," "right", respectively.

study four directions, considering the stability of the testing device. In addition, when the fixed bending angle of d$s$ = 0.02 mm is set, the light spot patterns in different bending directions are shown in Fig. 4(b). Even with the same bending angle, when the bending direction is different, the corresponding spot pattern can see significant differences due to the asymmetry of the fiber structure.

## 3.2. Deep learning assisted demodulation of multi-directional bending results

From the above results, it can be seen that the spot pattern of the DHF can describe the bending angles and directions, simultaneously. However, when relying solely on the light spot, it is difficult to quantitatively analyze the bending angle and direction. Although the movement of the interference fringes is easier to quantify compared to the speckle, multi-directional bending also has an impact on the direction and variation pattern of the fringe movement. In order to further solve this problem while considering the two-dimensional characteristics of the spot, the advanced 2D-CNN deep learning network[22] is used to train the network with the data of different bending angles and directions. The training model is shown in Fig. 5. First, 1280 sets of data (each set of data ranging from d$s$ equal to 0.01 mm to 0.09 mm, with the same d$s$ value corresponding to four different bending directions) are input into the model through image segmentation, with a single input image size of $100 \times 100$. Among them, the data of the training group accounts for 70%, the verification group accounts for 20%, and the test group accounts for 10%. Mini-batch size is 128, and the epoch is 100. The optimizer and learning rate drop factor (LRDF) are

"sgdm" and 0.5, respectively. After the first convolution layer (convolution kernel size is 3, and the number of filters is 8), the nonlinear activation function layer is used, and then the data is normalized. After that, it passes through the second convolution layer (convolution core size is 3, and the number of filters is 16) and then reaches the normalized data layer after passing through the nonlinear activation function. According to the data convolution processing module mentioned above, there are a total of four data convolution units in the network. Finally, through the full connection layer (output as a $1 \times 5$ vector, the five quantities are the connection between one-hot coding in four bending directions and angles), the output data is then subjected to classification (i.e., using the Softmax layer) and regression layers to achieve classification and recognition of the image bending direction and angle.

Figure 6 shows the root mean square error (RMSE) and loss value of the displayed training process. After the 35th round of model training, the RMSE value is basically about 0.90221, and the loss is lower, 0.4. The rest average accuracy of the validation data and test data is above 88%. Considering the judgment
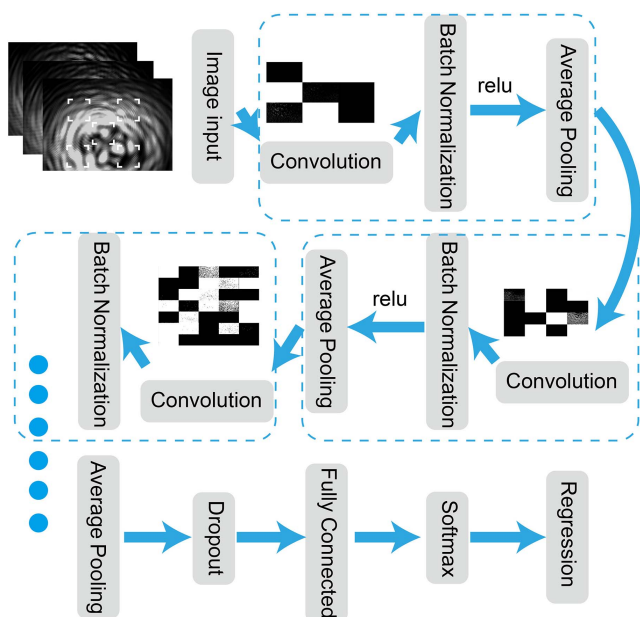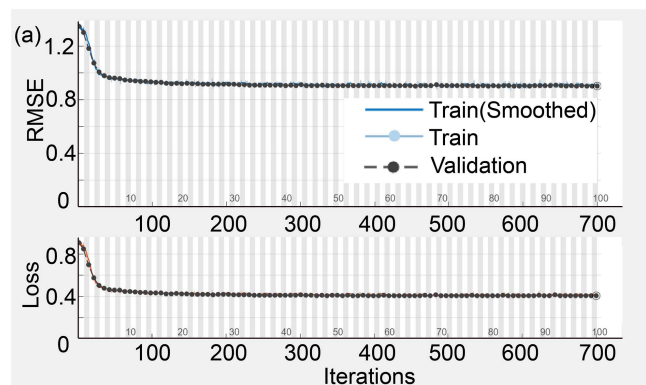


(b)

| Direction | Up | | | | Left | | | | Down | | | | Right | | | |
|---|---|---|---|---|---|---|---|---|---|---|---|---|---|---|---|---|
| | 0 | 0 | 0 | 1 | 0 | 0 | 1 | 0 | 0 | 1 | 0 | 0 | 1 | 0 | 0 | 0 |
| ds | 1-9 | | | | 1-9 | | | | 1-9 | | | | 1-9 | | | |
| Ac (Di&ds <0.6) | 98% | | | | 88% | | | | 90% | | | | 92% | | | |
| (Di&ds <0.4) | 94% | | | | 95% | | | | 99% | | | | 90% | | | |

(c)

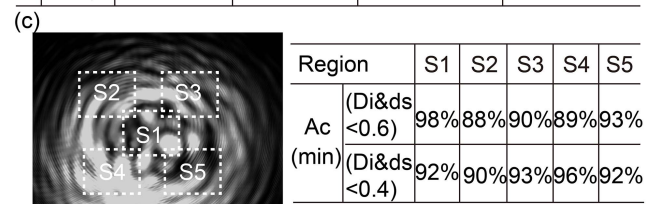| Region | | S1 | S2 | S3 | S4 | S5 |
|---|---|---|---|---|---|---|
| Ac (min) | (Di&ds <0.6) | 98% | 88% | 90% | 89% | 93% |
| | (Di&ds <0.4) | 92% | 90% | 93% | 96% | 92% |

**Fig. 6.** Deep learning network based on 2D-CNN for the multi-direction bending sensor demodulation results. (a) The root mean square error (RMSE) and loss of model training data and validation data. (b) Using the trained 2D-CNN model to verify the accuracy of the bending direction and bending angle for 128 sets of test data simultaneously. One-hot coding has been carried out in different directions. The 0.01–0.09 mm corresponding to d$s$ is also encoded as 1–9, which facilitates model convergence at the same scale of magnitude. (c) Accuracy verification after sampling different regions of the same input image.



**Fig. 5.** Deep learning network based on 2D-CNN for the multi-direction sensor prediction and the demodulation model. 1280 groups of spot data are input into the model according to the different feature areas of each group of data.

of different direction encoding and angle encoding in the model output, we adopted the judgment method shown in Fig. 6(b) for comprehensive accuracy estimation. Note that "Di" represents the output four-bit directional encoded vector value. Compare the labels of 128 test group data with the output values of the model, and verify the accuracy of the model in all directions when the difference is 0.4 and 0.6, respectively. There are differences in the accuracy estimates for the four directions. This is because the image segmentation sampling of the input image samples is not located at the center of the image, so the bending sensitivity of different regions and directions is different. Additionally, by adjusting the judgment threshold of the output results, the accuracy of the model can be improved to varying degrees. It should be pointed out that if the direction or bending angle is judged separately, the accuracy of the model can be higher than 99%. The accuracy here is to simultaneously consider both direction and bending angle. Since the accuracy varies among different regions, we divided the same sample into five regions S1, S2, S3, S4, and S5. The minimum accuracy [Ac (min)] for each region was calculated separately, and the results are shown in Fig. 6(c). It can be seen that the accuracy of the middle region S1 is higher under the same judgment rules. This is because the light field in the middle region can reflect the changes in each direction more evenly. So, compared to the edges, it can comprehensively reflect the information of the light field.

## 4. Conclusion

In summary, we have proposed a DHF multi-direction bending sensor. Due to the asymmetry of the fiber structure and the interference of the cladding beam, the perception of the direction and bending angle of the optical field distribution on the fiber end face is more obvious. By combining regression and classification models using convolutional neural network algorithms, simultaneous recognition of the bending angle and the direction can be achieved. Under the condition of determining the appropriate threshold setting, the accuracy of the test sample can reach up to 98%. Thus, the limitation of directional information obtained from the spectrum could be overcome, and information reuse is achieved from higher dimensions of the optical field information. All these characteristics indicate that the DHF spot pattern demodulation has potential application value in multi-dimensional vector sensing.

## Acknowledgement

## References

1. H. Xu, Y. Lu, J. X. Xiang, M. K. Zhang, Y. J. Zhao, Z. Y. Xie, and Z. Z. Gu, "A multifunctional wearable sensor based on a graphene/inverse opal cellulose film for simultaneous *in situ* monitoring of human motion and sweat," Nanoscale **10**, 2090 (2018).
2. L. Xie, Y. Wu, X. Liang, and P. Jin, "Bending behavior of inflatable structures filled with hydrogel beads," Powder Technol. **404**, 117473 (2022).
3. C. Li, D. Liu, C. Xu, Z. Wang, S. Shu, Z. Sun, W. Tang, and Z. L. Wang, "Sensing of joint and spinal bending or stretching via a retractable and wearable badge reel," Nat. Commun. **12**, 2950 (2021).
4. P. Lu, N. Lalam, M. Badar, B. Liu, B. T. Chorpening, M. P. Buric, and P. R. Ohodnicki, "Distributed optical fiber sensing: review and perspective," Appl. Phys. Rev. **6**, 041302 (2019).
5. W. Yang, Y. Ma, H. Sun, C. Huang, and X. Shen, "Molecularly imprinted polymers based optical fiber sensors: a review," TRAC Trends Anal. Chem. **152**, 116608 (2022).
6. M. Lai, Y. Zhang, Z. Li, W. Zhang, H. Gao, L. Ma, H. Ma, and T. Yan, "High-sensitivity bending vector sensor based on γ-shaped long-period fiber grating," Opt. Laser Technol. **142**, 107255 (2021).
7. M. Xu, J. Liu, L. Abbas, and A. Zhou, "High-sensitivity two-axis vector bending sensor based on side-grooved long period grating in eccentric core fiber," Opt. Laser Technol. **153**, 108218 (2022).
8. A. Yasli and H. Ademgil, "Bending analysis of multi-analyte photonic crystal fiber based surface plasmon resonance sensor," Opt. Quantum Electron. **54**, 205 (2022).
9. J. Villatoro, V. P. Minkovich, and J. Zubia, "Photonic crystal fiber interferometric vector bending sensor," Opt. Lett. **40**, 3113 (2015).
10. X. Zhu, Y. Pan, A. Sun, D. Sun, W. Liu, J. Cao, G. Zhang, Z. Han, L. Zou, Z. Liang, and Y. Shi, "High sensitivity curvature sensor based on a double-sphere tapered no-core fiber Mach–Zehnder interferometer," Opt. Laser Technol. **155**, 108364 (2022).
11. X. Yang, B. Luo, D. Wu, J. Fan, H. Gu, Y. Guo, and M. Zhao, "Highly sensitive curvature sensor based on a sandwich multimode fiber Mach–Zehnder interferometer," Opt. Express **30**, 40251 (2022).
12. Z. Y. Zhao, M. Tang, and C. Lu, "Distributed multicore fiber sensors," Opto-Electron. Adv. **3**, 190024 (2020).
13. A. I. Azmi, A. S. Abdullah, M. Y. Mohd Noor, M. H. Ibrahim, R. K. Raja Ibrahim, T. Tan, and J. Zhang, "Dynamic bending and rotation sensing based on high coherence interferometry in multicore fiber," Opt. Laser Technol. **135**, 106716 (2021).
14. Y. Tian, H. Dang, W. Liu, J. Cui, Y. Li, and J. Tan, "Structure shape measurement method based on optical fiber shape sensor," Meas. Sci. Technol. **34**, 085102 (2023).
15. Y. Zheng, P. Shum, S. Liu, B. Li, Y. Xiang, Y. Luo, Y. Zhang, W. Ni, Z. Wu, X. Q. Dinh, S. Zheng, J.-L. Auguste, and G. Humbert, "Experimental and numerical investigation on hollow core photonic crystal fiber based bending sensor," Opt. Express **27**, 30629 (2019).
16. J. Yang, F. Zou, C. Guan, P. Ye, S. Gao, Z. Zhu, P. Li, J. Shi, J. Yang, and L. Yuan, "Two-dimensional vector bending sensor based on a hole-assisted three-core fiber coupler," Opt. Lett. **47**, 5953 (2022).
17. Y. Meng, C. Fu, C. Du, L. Chen, H. Zhong, P. Li, B. Xu, B. Du, J. He, and Y. Wang, "Shape sensing using two outer cores of multi-core fiber based on OFDR," Proc. SPIE **12169**, 1216939 (2022).
18. H. Wang, L. Meng, Q. Xia, S. Yang, T. Yuan, X. Zhang, and L. Yuan, "3D parallel fiber Bragg gratings bending sensor based on single-channel measurement," IEEE Sens. J. **23**, 7599 (2023).
19. Q. Liang, J. Tao, X. Wang, T. Wang, X. Gao, P. Zhou, B. Xu, C. Zhao, J. Kang, L. Wang, C. Shen, D. Wang, and Y. Li, "Demodulation of Fabry–Perot sensors using random speckles," Opt. Lett. **47**, 4806 (2022).
20. J. Su, X. Dong, and C. Lu, "Characteristics of few mode fiber under bending," IEEE J. Sel. Top. Quantum Electron. **22**, 139 (2016).
21. M. H. Frosz, P. Roth, M. C. Günendi, and P. St.J. Russell, "Analytical formulation for the bend loss in single-ring hollow-core photonic crystal fibers," Photonics Res. **5**, 88 (2017).
22. C. Zuo, J. M. Qian, S. J. Feng, W. Yin, Y. X. Li, P. F. Fan, J. Han, K. Qian, and Q. Chen, "Deep learning in optical metrology: a review," Light Sci. Appl. **11**, 39 (2022).